Research Square

Preprints are preliminary reports that have not undergone peer review.
They should not be considered conclusive, used to inform clinical practice,
or referenced by the media as validated information.

Surrogate-driven end-to-end fabrication optimization for nanoimprinted free-form micro-optics in MicroLED HUDs

Wen-Di Li

liwd@hku.hk

University of Hong Kong https://orcid.org/0000-0002-7005-2784

Rongchen Qin

The University of Hong Kong

Zijie Jiang

The University of Hong Kong

Yaodong Wu

Shanghai Tianma Microelectronics

Shubin Huang

The University of Hong Kong

Jianwen Zhong

University of Hong Kong

Chuwei Liang

University of Hong Kong

Qijun Yao

qijun_yao@tianma.cn

Article

Keywords: Free-form cylindrical microlens array, Surrogate-driven end-to-end fabrication, Nanoimprint lithography, Direct laser writing, MicroLED head-up display

Posted Date: November 25th, 2026

DOI: https://doi.org/10.21203/rs.3.rs-11604421/v1

License: This work is licensed under a Creative Commons Attribution 4.0 International License.
Read Full License

Additional Declarations: There is no conflict of interest

Surrogate-driven end-to-end fabrication optimization for nanoimprinted free-form micro-optics in MicroLED HUDs

Rongchen Qin[1], Zijie Jiang[1], Yaodong Wu[2], Shubin Huang[1], Jianwen Zhong[1], Chuwei Liang[1], Qijun Yao[2] and Wen-Di Li [1, *]

[1] Department of Mechanical Engineering, University of Hong Kong, Hong Kong, China

[2] Shanghai Tianma Microelectronics, No. 889, Huiqing Rd, Pudong District, Shanghai, China

*liwd@hku.hk

ABSTRACT

Augmented-reality head-up displays demand compact light engines with high directional luminance. MicroLEDs have excellent brightness, but their inherent Lambertian emission pattern demands precise micro-optical elements for beam reshaping. In this work, free-form cylindrical microlens arrays (FCMLAs) are demonstrated for the collimation and redirection of MicroLED emission. The combination of grayscale direct laser writing (DLW) and ultraviolet nanoimprint lithography (UV-NIL) is adopted to support scalable fabrication of the designed FCMLAs. Since a multi-step fabrication process normally introduces a deviation between the design and the fabricated morphology, to efficiently calibrate and optimize the complete fabrication process, we demonstrate a surrogate-driven end-to-end framework that treats the DLW and UV-NIL process as a fabrication black box. The framework learns the relation between the grayscale map and the final imprinted profile directly from experimental measurements. Gaussian process regression (GPR) captures the nonlinear process response, while proportional-type iterative learning control (P-type ILC) drives rapid convergence to the target. The framework reduces the profile RMSE from 2.052 μm for the initial contrast-curve result to 0.21 μm for the final profile in only two experimental steps. Batch-fabricated FCMLAs show an average relative profile deviation below 2%. After integration with MicroLEDs, the FCMLA produces a 2.65-fold peak-intensity enhancement at the designed emission angle of 20°, with a luminance of 9.3×10^4 nits. The light engine with $20 cm^3$ volume is two orders of magnitude smaller than conventional HUD systems. This work provides a route for effectively translating free-form micro-optical designs from laboratory prototypes to scalable manufacturing.

Keywords: Free-form cylindrical microlens array, Surrogate-driven end-to-end fabrication, Nanoimprint lithography, Direct laser writing, MicroLED head-up display

INTRODUCTION

Augmented-reality head-up displays (AR-HUDs) are emerging as an important human-machine interface for vehicles(*1, 2*). Their optical engines must deliver bright information within the driver's eyellipse while remaining compact and energy efficient(*3-6*). These requirements impose a persistent trade-off among directional luminance, optical efficiency, and system volume.

Micro-light-emitting diodes (MicroLEDs) are attractive sources for AR-HUDs (*7*) because of their high brightness, fast response, and reliability(*8, 9*). However, their Lambertian emission is poorly matched to the limited acceptance angle of HUD optics(*10*), leaving much of the emitted power outside the useful angular range(*11*). Optical elements are therefore required to collect and redirect the divergent emission(*12, 13*). However, conventional multi-element systems increase volume and interface loss(*14, 15*), while symmetric microlens arrays require source tilt and introduce alignment constraints(*16*). Metasurfaces can provide collimation and off-axis emission, but chromatic dispersion and fabrication throughput remain practically challenging (*17, 18*). To simultaneously achieve compactness and high directional luminance, free-form micro-optics can be integrated with MicroLEDs to control their Lambertian emission. In particular, free-form cylindrical microlens arrays (FCMLAs) provide an efficient solution through their continuous asymmetric profiles(*19-22*). Each free-form cylindrical microlens can collimate light from a single MicroLED pixel and redirect it before the beam enters the downstream HUD optics.

In the present system, each FCMLA element is aligned with one MicroLED pixel to redirect the emitted light toward 20° off the normal (Fig. 1A, B). The windshield then guides the beam into the driver's field of view. The integrated light engine occupies 20 cm^3, compared with approximately 10 L for conventional HUD systems(*14*). Manufacturing this device requires high-throughput fabrication of high-sag free-form profiles with controlled final morphology. Thermal reflow provides high throughput but mainly produces symmetric or near-spherical surfaces(*23-25*). Grayscale DLW can define continuous free-form profiles(*26, 27*), however, slow serial writing limits its use in volume production(*28*). Precision mechanical machining is similarly constrained by serial processing and production cost(*29, 30*). Combining DLW master fabrication with multi-step UV-NIL replication therefore provides a scalable route to large-area FCMLA production(*31, 32*).

The deviation between the designed profile and the fabricated device is normally large in a multi-step fabrication process(*33*). Practical accuracy therefore depends on correcting the deviation. The conventional correction method of the nanoimprint process seeks to minimize deviations by producing a master mold close to the target profile and then maintaining high-fidelity replication through subsequent transfer steps(*34, 35*). This method suffers from low efficiency due to the accumulation of fabrication errors across multiple steps, including nonlinear photoresist development, curing shrinkage, demolding deformation, and stamp compliance(*36-38*).

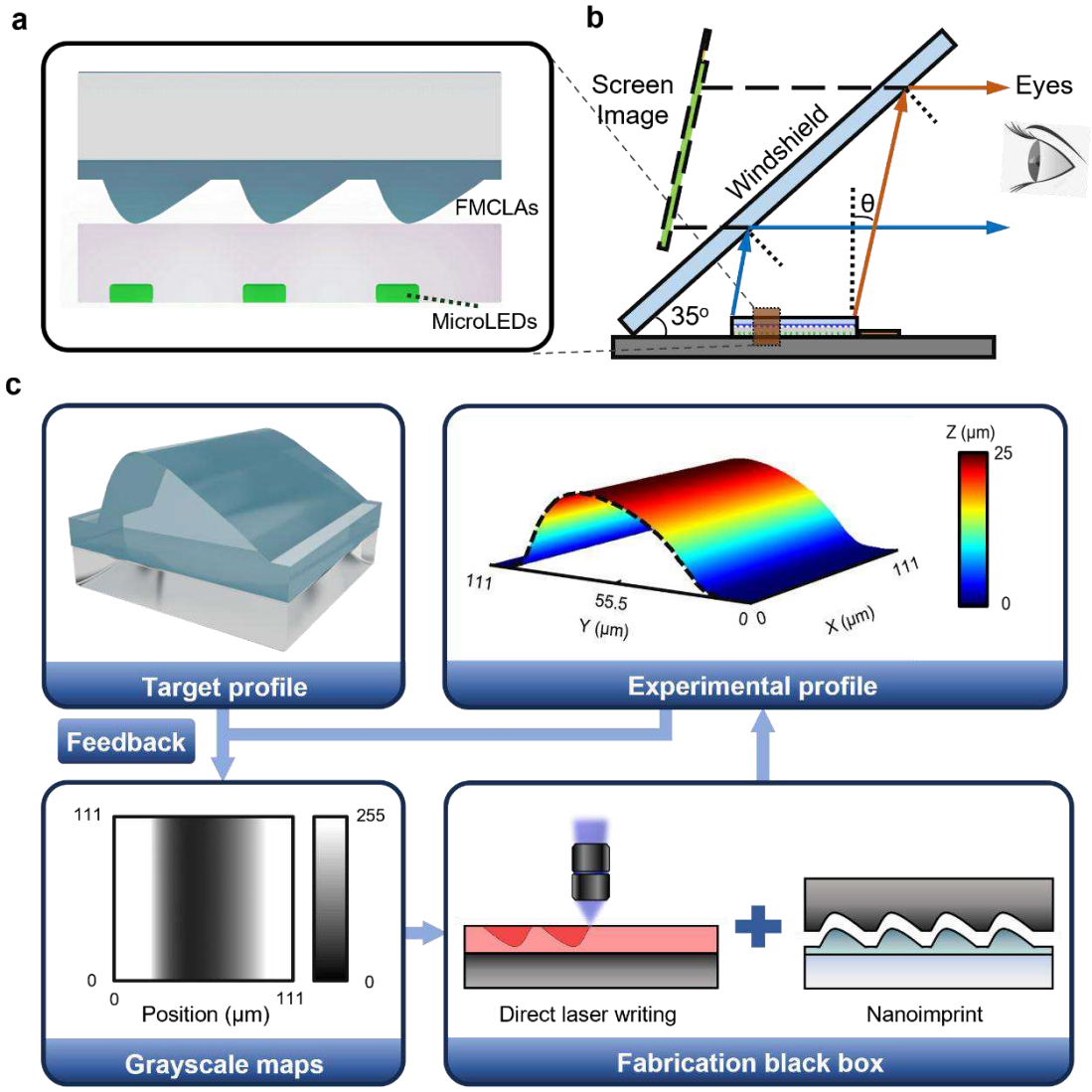

Fig. 1. Schematic illustration of free-form cylindrical microlens array (FCMLA) application and fabrication. (A) Integration of an FCMLA on a MicroLED display for directional luminance enhancement. **(B)** Optical path configuration of a window-type automotive head-up display employing the FCMLA. **(C)** Flowchart of the surrogate-driven end-to-end fabrication framework. The final imprinted profile is used to update the grayscale map while the intermediate steps are treated as a fabrication black box.

Instead of inefficiently optimizing each step, we represent the complete DLW and UV-NIL route as a black-box function from the grayscale map to the final imprinted profile. Surrogate models are well suited to this task because they approximate implicit input-output relations directly from evaluated samples. They can replace simulations that are difficult, computationally expensive, or time-consuming(*33, 39-41*). We choose a GPR model to estimate the nonlinear

response of the fabrication black box, as it combines nonlinear interpolation with predictive uncertainty and performs effectively with compact experimental datasets(*42-44*). P-type ILC then updates the grayscale map from the measured residual error to accelerate target-specific convergence(*45, 46*).

This work presents a surrogate-assisted end-to-end fabrication framework for multi-step manufacturing of micro-optics (Fig. 1C). The framework learns the complete process response from experimental final profiles without resolving each intermediate step. The profile RMSE decreased from 2.052 μm to 0.21 μm after correction. Multi-step UV-NIL produced large-area FCMLAs with an average relative profile deviation below 2%. After post-integration with MicroLEDs(*47*), the FCMLA increased peak intensity at the target angle of 20° by a factor of 2.65, demonstrating compact off-axis beam steering for AR-HUDs. This work establishes a scalable manufacturing route for translating free-form micro-optics from computational design to practical optical systems.

RESULTS

Stepwise fabrication and integration

The physical implementation of the end-to-end optimization framework relies on a robust and scalable stepwise fabrication and integration process detailed in Fig. 2. This process delineates the complete physical steps from grayscale direct laser writing (DLW) of the master mold to the final device imprinting and integration, establishing a stable and repeatable manufacturing foundation for the entire optimization cycle.

The fabrication starts with patterning a master mold via high-resolution grayscale DLW on photoresist, defining the continuous surface relief of the cylindrical microlens (Fig. 2A). The DLW equipment enables 12-bit (4096-level) discrete exposure control, enabling precise modulation of the local exposure dose and, consequently, the developed photoresist depth. This allows for the direct writing of smooth, continuous three-dimensional profiles that are essential for high-quality optical surfaces. Since positive photoresist is employed for DLW patterning, the master mold is fabricated with a profile complementary to the target.

A three-step UV-NIL process is then employed. The first imprint creates an intermediate working stamp I (Fig. 2B), the second imprint yields a complementary working stamp II (Fig. 2C), and the final imprint replicates the functional microlens array on a glass substrate (Fig. 2D, E). The three-step imprint strategy is critical for protecting the original DLW master and providing multiple reusable working stamps. OrmoStamp (Micro resist technology GmbH, Berlin, Germany) was used for the robust working stamps (I and II), while OrmoClear FX from the same supplier, with its high transparency and glass-like properties after curing, was used for the final device.

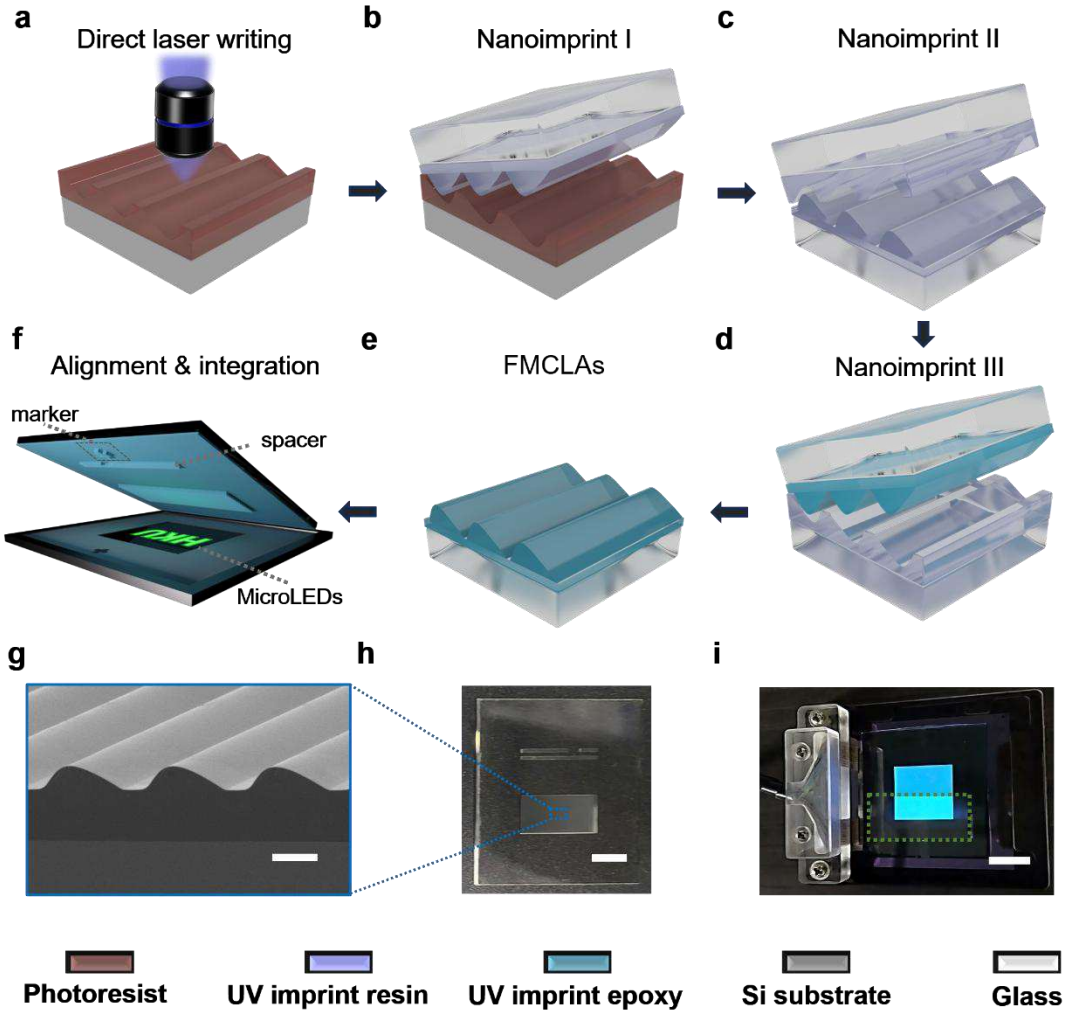

Fig. 2. Fabrication and integration of FCMLAs. (A) Master mold patterning via grayscale lithography using 12-bit direct laser writing. **(B)** First UV nanoimprint lithography (UV-NIL) step to create working stamp I using UV-curable resin. **(C)** Second UV-NIL step producing working stamp II with structures complementary to the final FCMLAs. **(D)** Third UV-NIL step using UV-imprint epoxy. **(E)** Final functional FCMLA device. **(F)** Integration schematic of the FCMLA onto MicroLEDs, using cross-markers for alignment and spacers to support lens-free regions. **(G)** Scanning electron microscope (SEM) image of the free-form cylindrical microlens array. **(H)** Optical photograph of an imprinted FCMLA device. **(I)** Photograph of the final integrated device, with the FCMLA-covered area highlighted by a green dashed box. Scale bars: 50 μm (G), 1 cm (H), and 1 cm (I).

The integration of the microlens array with the MicroLED chip employs alignment markers and spacers to simultaneously ensure lateral alignment accuracy and vertical spacing uniformity

(Fig. 2F). To achieve recognizable markers without introducing additional materials or process steps, the alignment pattern is designed as arrays of "moth-eye-like" micropatterned structures. These structures appear dark in transmission-mode imaging after imprinting, providing excellent contrast and full compatibility with high-throughput imprinting (see Supplementary Note S2). Meanwhile, spacers with precisely defined heights are distributed across the blank regions to maintain a uniform air gap between the FCMLA and the MicroLED chip. This configuration not only prevents unintended contact but also effectively suppresses device tilting, thereby ensuring mechanical stability and optical consistency of the integrated device.

Photographs and micrographs of the final integrated device (Fig. 2G-I) confirm the successful large-area replication and the excellent structural integrity of the FCMLA. The SEM image shown in Fig. 2G illustrates the uniform and smooth surface of the microlenses. The camera image (Fig. 2H) shows a uniform, defect-free array over the device area. The photograph of the fully integrated device (Fig. 2I) provides a macroscopic view of the FCMLA-on-MicroLED assembly. A green dashed box marks the FCMLA-covered device area, clearly showcasing the exact alignment and effective scalability of the integration process.

The scalability of this NIL process is inherently supported by reusable Working Stamps I and II, which are crucial for transitioning from laboratory prototyping to volume manufacturing. Working stamp II, which carries the inverse of the final lens profile, maintained the morphology of the replicated FCMLAs without obvious degradation after eleven consecutive imprints. This approach establishes a clear route to high-volume production, meeting the throughput demands of the display industry.

Fabrication deviation and end-to-end optimization

We first evaluated a grayscale map (Fig. 3A) generated directly from the photoresist contrast curve (Supplementary Fig. S1). Cross-sectional SEM images (Fig. 3B) and extracted profiles (Fig. 3C) revealed two sources of deviation. Firstly, the DLW master differed from the target, showing that the contrast curve did not fully describe the high-sag free-form surface. Contrast curves are calibrated using uniform test patterns, and therefore cannot fully capture the proximity effects and nonlinear process response inherent to high-sag free-form surfaces. Secondly, the profile changed further through the three-step UV-NIL transfer chain. As shown in Fig. 3C, the final imprinted morphology (green square line) differed from the master (purple line). Related studies have also reported shrinkage and replication errors after imprinting(*36-38, 48*). The maximum absolute deviation and RMSE of the final profile were 4.56 μm and 2.052 μm, respectively. These observations experimentally demonstrated the necessity for an end-to-end optimization strategy.

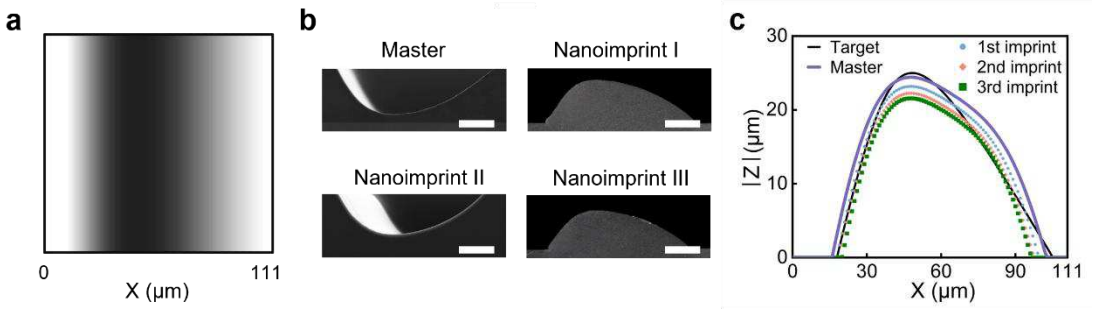

Fig. 3. Initial fabrication result obtained from contrast-curve-based grayscale design. (A) Initial grayscale map for the FCMLA generated from the calibrated photoresist contrast curve. **(B)** Cross-sectional SEM images of the DLW-patterned master and the sequential UV-NIL transfer results. **(C)** Profile evolution during the fabrication process. The black solid line represents the absolute value of the target profile, the purple line represents the absolute value of the master profile, and the other lines represent the absolute value of the sequentially imprinted profiles. Scale bars: 20 μm (B).

The end-to-end optimization progresses through two steps, consisting of surrogate-driven black-box estimation and rapid ILC convergence (workflow shown in Fig. 4A). Each updated grayscale map defines the exposure dose distribution for fabricating a new master mold by DLW. The master profile is then transferred through the nanoimprint process, and the measured final imprinted profile is used to update the dose map for the next iteration. During the first step ($k = 1$), five grayscale maps were generated to train the surrogate model by randomly perturbing the initial design shown in Fig. 3A. Each map was fabricated through the fixed DLW and UV-NIL process, and its final imprinted profile was measured. Two representative grayscale maps and their final profiles are shown in Fig. 4B, C, E, and F. GPR was selected as the surrogate to capture the implicit relation between the grayscale map and the final imprinted profile. The GPR-generated map (Fig. 4D) was used to produce the profile in Fig. 4G. The maximum absolute deviation and RMSE significantly decreased to 2.41 μm and 0.97 μm, respectively (blue stars in Fig. 4I).

During the second step ($k > 1$), P-type ILC efficiently corrected the residual error between the measured GPR profile and the target. The profile difference, scaled by the learning gain, was applied to update the grayscale map. After ILC correction, the maximum absolute deviation and RMSE of the final profile (Fig. 4H) were substantially reduced to 0.46 μm and 0.21 μm, respectively (red spots in Fig. 4I). GPR therefore provided the process-aware initialization, while P-type ILC rapidly removed the remaining target-specific error.

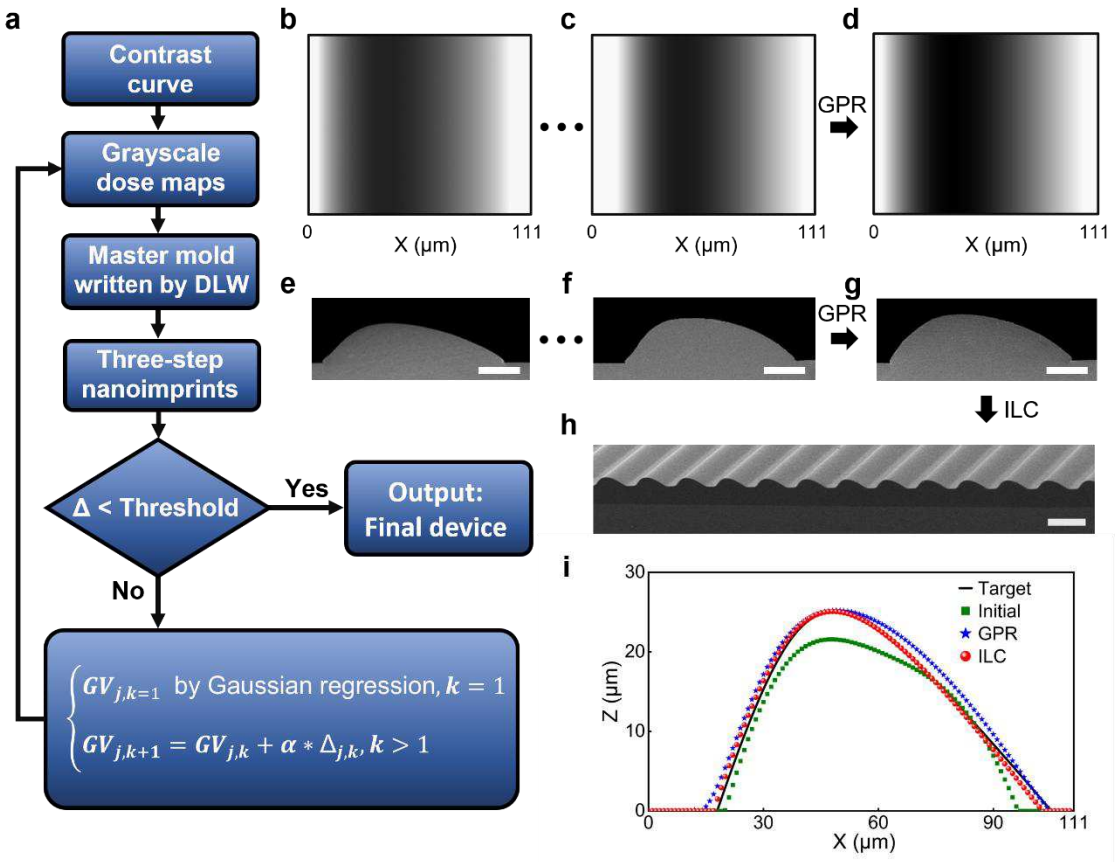

Fig. 4. Surrogate-driven end-to-end correction of the FCMLA fabrication process. (A) Workflow of the surrogate-driven end-to-end fabrication optimization. **(B** and **C)** Two representative grayscale maps from the training set. **(D)** Grayscale map generated by GPR. **(E** and **F)** Final imprinted profiles corresponding to the grayscale maps in (B and C). **(G)** Final imprinted profile obtained from the GPR-generated grayscale map in (D). **(H)** Final imprinted profile after one P-type ILC correction. **(I)** Profile evolution during optimization. The black line is the target profile. Green squares show the initial contrast-curve-based result, blue stars show the GPR-initialized result, and red spots show the result after one ILC correction. Scale bars are 20 μm in **(E-G)** and 100 μm in **(H)**.

Batch replication and optical validation

Leveraging the optimized and highly stable process described above, we further demonstrated batch fabrication capability and morphological uniformity (Fig. 5A). Using a single working stamp II, we continuously produced over ten identical FCMLA devices on 4-inch glass substrates. As shown in the photograph, all devices exhibit good macroscopic consistency and are free of visible defects, providing a direct visual indication of the stability and repeatability of intra-batch process

parameters.

Three-dimensional surface profiling of microlenses at the center of the first imprinted array confirms the high-fidelity replication of the designed free-form curvature (Fig. 5B, C). The optical micrograph (Fig. 5B) shows the top view of cylindrical lens elements. The 3D surface map acquired by white-light interferometry (Fig. 5C) displays the smooth, continuous, and characteristic free-form sag profile.

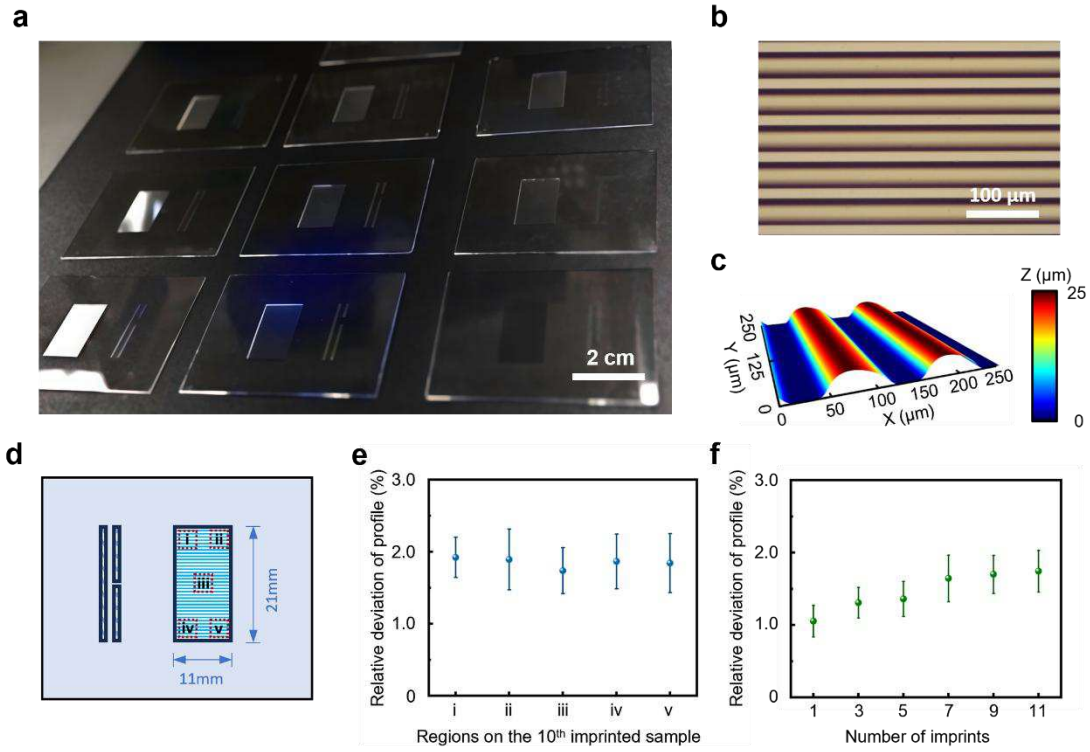

Fig. 5. Morphological characterization of batch-fabricated FCMLAs. (A) Photograph of multiple FCMLA devices produced via batch nanoimprint lithography. **(B)** Optical micrograph of a free-form cylindrical microlens at the center of the first imprinted device. **(C)** Three-dimensional surface profile of the fabricated free-form cylindrical microlens at the center of the first imprinted device. **(D)** Layout of a single FCMLA device, showing the spacers on the left and the functional microlens array (11 × 21 mm²) on the right. **(E)** Relative profile deviation of the fabricated FCMLA across different sampling regions on the tenth imprinted device, with the region numbers corresponding to the labels in (D). **(F)** Relative profile deviation at the center of the FCMLAs versus the number of imprint cycles.

A statistical analysis of profile deviation across five distinct sampling regions (four corners and the center) within a single 11 × 21 mm² device from the tenth imprinting cycle (Fig. 5D) revealed that excellent spatial uniformity was well maintained (Fig. 5E). The relative deviation was lowest

at the center (mean: 1.74%, fluctuation: 0.16%) and highest at the top-left corner (1.92%). The average relative deviation across all five regions was 1.85%. These consistently low deviation values indicate that the NIL process maintains excellent pressure and resin flow uniformity over a large area even after multiple imprinting cycles, which is critical for ensuring consistent optical performance from every microlens in the array.

The process robustness is further demonstrated by the consistent profile fidelity maintained over multiple consecutive imprinting cycles using the same working stamp (Fig. 5F). The relative deviation at the device center for the 1st, 3rd, 5th, 7th, 9th, and 11th imprints was 1.05%, 1.31%, 1.36%, 1.64%, 1.70%, and 1.75%, respectively. Although a gradual increase was observed, the deviation remained within a narrow range, with a standard deviation of approximately 0.28% across the measured cycles. This demonstrates the effectiveness of the imprint recipe (see Methods) and indicates that the stamp possesses sufficient mechanical durability for sustained use in batch production.

After the high-precision, high-uniformity batch fabrication, we then turned to a systematic evaluation of the optical performance by employing both simulation and experiment. First, a ray-tracing simulation based on the actual profile parameters of the fabricated devices was performed to visualize their beam-steering function (Fig. 6A). The source model in the simulation was constructed from experimentally measured emission characteristics of the MicroLEDs. The incident rays were concentrated and collectively deflected to the target angle of 20°. This theoretically confirms the directional emission capability of the microlens and predicts the expected angular shift.

Imaging performance of integrated devices

To validate the optical performance, experimental characterization of the angular emission profiles was performed quantitatively using a custom goniophotometer (Fig. 6B). The measurement setup employed a rotating detector to record the angular distribution of luminous intensity in the far field. The MicroLED chip was driven at a constant current, with measurements taken first through a plain cover glass and then through the integrated FCMLAs.

Upon integration of the microlens array, the experimental results demonstrated directional enhancement. The normalized intensity at the target angle of 20° increased from 0.23 for the bare MicroLED to 0.61, corresponding to a 2.65-fold enhancement (Fig. 6C). The peak luminance at 20° attained 9.3×10^4 nits. The measured red line in Fig. 6C had a full width at half maximum (FWHM) of 21.4° between 9.9° and 31.3°. The calculated deflection efficiency, defined as the fraction of total emitted flux redirected into a target angular cone, reached 25.77% within the ±5° cone (15° to 25°) and 50.80% within the ±10° cone (10° to 30°). The experimentally measured angular intensity profile followed the overall trend predicted by the ray-tracing simulation (green

dots in Fig. 6C), although the measured values were slightly lower than the simulated results. The difference may arise from practical factors excluded in the simulation model, such as optical losses and deviations introduced during bonding. Nonetheless, the experimental data convincingly support the validity of the device design and the accuracy of the fabrication framework for beam-shaping.

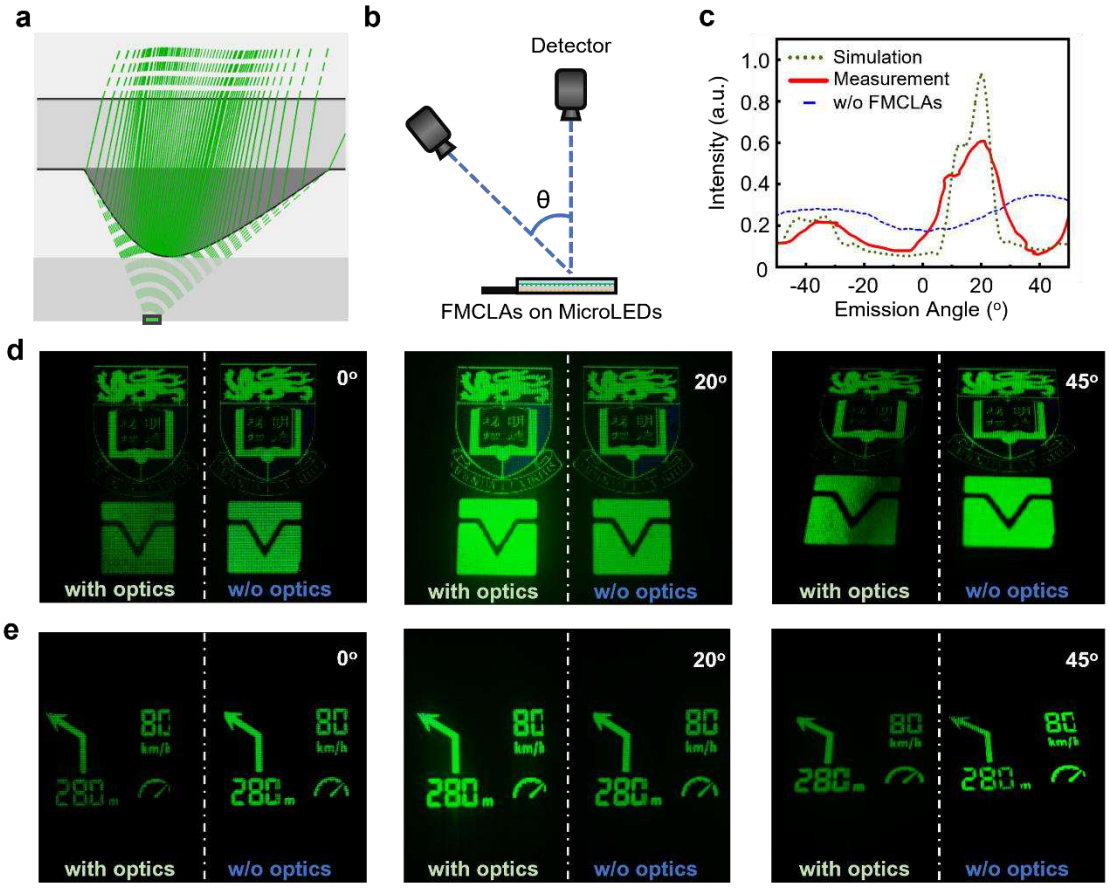

Fig. 6. Optical characterization and imaging test of the FCMLAs. (A) Ray-tracing simulation of the FCMLA. **(B)** Schematic of the experimental setup for measuring the angular distribution of light intensity. **(C)** Measured and simulated angular intensity distributions. Green dots show the simulation, the red line shows the measurement with the FCMLAs, and the blue dashed line shows the measurement without the FCMLAs. **(D)** Images of institutional logos displayed on the MicroLED panel. **(E)** Images of typical HUD informational graphics (e.g., speed, distance, and turn indicators). For both (D) and (E), images were captured at viewing angles (θ) of 0°, 20°, and 45°. The left and right halves correspond to the areas with and without the integrated FCMLA, respectively, separated by a white dotted line.

Visual imaging tests provide intuitive evidence of directional enhancement. As shown in Fig. 6D and E, images of institutional logos and typical HUD graphics displayed on the MicroLED

panel were captured at viewing angles (θ) of 0°, 20°, and 45°. In each image, the left and right halves correspond to the areas with and without the integrated FCMLA, respectively. At the target angle of θ = 20°, the patterns on the FCMLA side appear noticeably brighter, confirming the focused emission. Conversely, at θ = 45°, the brightness contrast reverses, with the reference side becoming brighter (additional demonstration images are provided in Supplementary Fig. S3). This visual outcome directly corroborates the quantitative goniophotometric data, demonstrating that the FCMLA successfully creates a distinct target viewing region by redirecting luminous output toward the target angle.

DISCUSSION

This work establishes a surrogate-driven end-to-end fabrication framework for FCMLAs applied in MicroLED-based HUDs. The complete fabrication process is treated as a black box. In the framework, GPR is selected as the surrogate model to estimate the implicit process response, while P-type ILC efficiently removes the remaining target-specific error. The current implementation utilizes a constant ILC gain, but a spatially varying gain could be employed in the future to further reduce overcorrection(*49*). Even with a constant gain, the profile RMSE of fabricated devices was significantly reduced from 2.052 μm to 0.21 μm. In addition, the scalable fabrication method produced 11 × 21 mm² FCMLAs with an average relative profile deviation of 1.85% and consistent profiles over multiple imprint cycles. After integration, the normalized intensity at 20° increased 2.65-fold, and the luminance reached 9.3×10^4 nits. The deflection efficiencies were 25.77% within ±5° and 50.80% within ±10°. This work demonstrated a scalable fabrication solution for compact light engines applied in MicroLED-based HUDs. More broadly, the framework provides a general correction framework between computational design and practical manufacturing for various functional micro-optics.

METHODS

Optical design and simulation

The free-form cylindrical microlens was designed in two steps using an in-house Python program. First, an initial cross-sectional profile was calculated for the finite MicroLED source and fitted with an eighth-order even polynomial. In the second step, ray tracing was used to simulate light propagation through the MicroLED–FCMLA system. The predicted brightness at the target angle of 20° served as the optimization objective, and gradient descent was used to update the polynomial coefficients. Further details of the design method are provided in Supplementary Note

S3.

Master mold fabrication via direct laser writing

The master was patterned in a 30-μm-thick layer of grayscale photoresist (ma-P 1275G, Micro resist technology GmbH, Berlin, Germany) on a 4-inch silicon wafer using a 12-bit direct laser writing system (PicoMaster 200, RAITH Laser Systems B.V., Eindhoven, the Netherlands). The pattern was exposed with a spot size of approximately 450 nm, a step size of 300 nm, a scan speed of 200 mm/s, and a base dose of 860 mJ/cm² modulated by a 12-bit grayscale map. After exposure, the resist was baked at 110 °C for 10 min and developed in ma-D 532/S (Micro resist technology GmbH, Berlin, Germany) for 5 min.

UV-nanoimprint lithography process

The three-step UV-NIL process was performed using a custom-built nanoimprinter. OrmoStamp and OrmoClear FX (Micro resist technology GmbH, Berlin, Germany) were used for the working stamps and the final device on a 300-μm-thick glass substrate, respectively. Each imprint was performed under controlled pressure with a UV dose of 1000 mJ/cm² at 365 nm. The working stamps were treated by vapor-phase deposition of 1H,1H,2H,2H-perfluorodecyltrichlorosilane (FDTS) for 5 min at 100 °C under vacuum. Resin volume was regulated locally with a patterned screen-printing stencil before imprinting to promote uniform filling and prevent overflow.

Surrogate-driven end-to-end optimization algorithm

Five training grayscale maps were generated by applying random perturbations to the contrast-curve-based design. Each map was fabricated through the complete process. The grayscale map and its final imprinted x-z profile served as the corresponding GPR input and output, respectively.

GPR with a radial basis function kernel and P-type ILC were implemented in Python. The GPR model was trained with the five pairs of the grayscale maps and corresponding final profiles described above. The ILC update law was $GV_{j,k+1} = GV_{j,k} + \alpha \cdot \Delta_{j,k}$, where $GV_{j,k}$ and $\Delta_{j,k}$ denotes the gray value and the profile error at position j in iteration k, respectively. The learning gain α was set to 0.36, and $\Delta_{j,k}$ denotes the profile difference. The GPR-generated grayscale map was used for one P-type ILC correction. Optimization ended when the RMSE between the final imprinted and target profiles was below 500 nm.

Optical and morphological characterization

Angular intensity distributions of the display were measured with a motorized 6-axis

goniometer (DMS 803, Konica Minolta). Surface profiles and roughness were analyzed using a confocal laser microscope (LEXT OLS 4000, Olympus) and a scanning electron microscope (Sigma 300, Zeiss).

Supplementary Information

Supplementary Notes S1 to S3
Figs. S1 to S3

Acknowledgements

This study was supported by the Research Grants Council of the Hong Kong SAR through General Research Fund (Award Nos. 17209320 and 17205524) and the Innovation and Technology Fund (Award No. GHP/259/22). The authors would also like to thank the Central Fabrication Laboratory of the University of Hong Kong for their assistance with sample fabrication.

Author contributions

W.-D.L. supervised the whole project. W.-D.L., R.-C.Q., and Z.-J.J. conceived the fabrication experiments. R.-C.Q., Z.-J.J., and J.-W.Z. constructed the experimental setups. R.-C.Q. carried out the experiments. Y.-D.W. and Q.-J.Y designed the device. Y.-D.W. and R.-C.Q. developed the numerical methods for simulation. R.-C.Q. and S.-B.H completed the morphological measurement. Y.-D.W. and Q.-J.Y. performed the optical characterization. All authors participated in the writing of the manuscript.

Competing interests

The authors declare no competing interests.

Data availability

The data that support the findings of this study are available from the corresponding author upon reasonable request.

References

1. J. Skirnewskaja, T. D. Wilkinson, Automotive holographic head-up displays. *Advanced materials* **34**, 2110463 (2022).
2. H. S. Park, M. W. Park, K. H. Won, K. H. Kim, S. K. Jung, In-vehicle AR-HUD system to provide driving-safety information. *ETRI journal* **35**, 1038–1047 (2013).
3. Y. Inuzuka, Y. Osumi, H. Shinkai, in *Proceedings of the Human Factors Society Annual Meeting*. (SAGE Publications Sage CA: Los Angeles, CA, 1991), vol. 35, pp. 1574–1578.
4. Y. Liu, J. Dong, Y. Qiu, B.-R. Yang, Z. Qin, Compact dual-focal augmented reality head-up display using a single picture generation unit with polarization multiplexing. *Optics express* **31**, 35922–35936 (2023).
5. G. Dai, H. Yang, L. Yin, K. Ren, J. Liu, X. Zhang, J. Zhang, Compact pupil-expansion AR-HUD based on surface-relief grating. *Optics Express* **32**, 6917–6928 (2024).
6. J. Skirnewskaja, "High-Definition Holographic Head-Up Displays", thesis, University of Cambridge (United Kingdom) (2024).
7. C. T. Draper, C. M. Bigler, M. S. Mann, K. Sarma, P.-A. Blanche, Holographic waveguide head-up display with 2-D pupil expansion and longitudinal image magnification. *Applied optics* **58**, A251–A257 (2019).
8. P. J. Parbrook, B. Corbett, J. Han, T. Y. Seong, H. Amano, Micro-light emitting diode: from chips to applications. *Laser & Photonics Reviews* **15**, 2000133 (2021).
9. W. C. Miao, F. H. Hsiao, Y. Sheng, T. Y. Lee, Y. H. Hong, C. W. Tsai, H. L. Chen, Z. Liu, C. L. Lin, R. J. Chung, Microdisplays: mini-LED, micro-OLED, and micro-LED. *Advanced Optical Materials* **12**, 2300112 (2024).
10. E. Chen, Z. Fan, K. Zhang, C. Huang, S. Xu, Y. Ye, J. Sun, Q. Yan, T. Guo, Broadband beam collimation metasurface for full-color micro-LED displays. *Optics Express* **32**, 10252–10264 (2024).
11. Y. Liu, T. Xia, A. Du, T. Liang, Z. Fan, E. Chen, J. Sun, Q. Yan, T. Guo, Omnidirectional color shift suppression of full-color micro-LED displays with enhanced light extraction efficiency. *Optics Letters* **48**, 1650–1653 (2023).
12. C. Wang, Y. Fan, B. Wang, H. Yang, J. Shao, Fully Enclosed Composite Micro/Nano-Package for High-Quality Micro-LED Display Pixels and In Situ Nanoimprint Technology. *Advanced Materials Technologies* **9**, 2301782 (2024).
13. E. Quesnel, A. Lagrange, M. Vigier, M. Consonni, M. Tournaire, V. Le Marchand, A. Suhm, P. Demars, J. C. Pillet, B. Ben Bakir, Dimensioning a full color LED microdisplay for augmented reality headset in a very bright environment. *Journal of the Society for Information Display* **29**, 3–16 (2021).
14. Z. Qin, S.-M. Lin, K.-T. Luo, C.-H. Chen, Y.-P. Huang, Dual-focal-plane augmented reality head-up display using a single picture generation unit and a single freeform mirror. *Applied*

optics **58**, 5366–5374 (2019).

15. Z. Qin, F.-C. Lin, Y.-P. Huang, H.-P. D. Shieh, Maximal acceptable ghost images for designing a legible windshield-type vehicle head-up display. *IEEE Photonics Journal* **9**, 1–12 (2017).
16. M. K. Hedili, M. O. Freeman, H. Urey, Microlens array-based high-gain screen design for direct projection head-up displays. *Applied optics* **52**, 1351–1357 (2013).
17. J. Huang, Z. Hu, X. Gao, Y. Xu, L. Wang, Unidirectional-emitting GaN-based micro-LED for 3D display. *Optics Letters* **46**, 3476–3479 (2021).
18. E. Khaidarov, Z. Liu, R. Paniagua-Domínguez, S. T. Ha, V. Valuckas, X. Liang, Y. Akimov, P. Bai, C. E. Png, H. V. Demir, Control of LED emission with functional dielectric metasurfaces. *Laser & Photonics Reviews* **14**, 1900235 (2020).
19. T.-W. Lin, C.-F. Chen, J.-J. Yang, Y.-S. Liao, A dual-directional light-control film with a high-sag and high-asymmetrical-shape microlens array fabricated by a UV imprinting process. *Journal of Micromechanics and Microengineering* **18**, 095029 (2008).
20. Y.-P. Huang, J.-J. Chen, F.-J. Ko, H.-P. D. Shieh, Multidirectional asymmetrical microlens array light control film for improved image in reflective color liquid crystal displays. *Japanese journal of applied physics* **41**, 646 (2002).
21. L.-L. Ma, S.-B. Wu, W. Hu, C. Liu, P. Chen, H. Qian, Y. Wang, L. Chi, Y.-q. Lu, Self-assembled asymmetric microlenses for four-dimensional visual imaging. *ACS nano* **13**, 13709–13715 (2019).
22. J. Wojtanowski, M. Traczyk, Optical design of transmitter lens for asymmetric distributed free space optical networks. *Optics & Laser Technology* **101**, 319–327 (2018).
23. J. Qiu, M. Li, H. Ye, J. Zhu, C. Ji, Fabrication of high fill-factor microlens array using spatially constrained thermal reflow. *Sensors and Actuators A: Physical* **279**, 17–26 (2018).
24. Z.-J. Lian, S.-Y. Hung, M.-H. Shen, H. Yang, Rapid fabrication of semiellipsoid microlens using thermal reflow with two different photoresists. *Microelectronic engineering* **115**, 46–50 (2014).
25. H. Yang, C.-K. Chao, M.-K. Wei, C.-P. Lin, High fill-factor microlens array mold insert fabrication using a thermal reflow process. *Journal of micromechanics and microengineering* **14**, 1197 (2004).
26. C. R. Ocier, C. A. Richards, D. A. Bacon-Brown, Q. Ding, R. Kumar, T. J. Garcia, J. Van De Groep, J.-H. Song, A. J. Cyphersmith, A. Rhode, Direct laser writing of volumetric gradient index lenses and waveguides. *Light: Science & Applications* **9**, 196 (2020).
27. S. Luan, F. Peng, G. Zheng, C. Gui, Y. Song, S. Liu, High-speed, large-area and high-precision fabrication of aspheric micro-lens array based on 12-bit direct laser writing lithography. *Light: Advanced Manufacturing* **3**, 676–686 (2022).

28. X. Liu, Q. Liu, M. Luo, L. Xu, C. Kuang, X. Liu, Super-resolution direct laser writing via multiphoton and peripheral photoinhibition photolithography. *Optics Letters* **50**, 1675–1678 (2025).
29. H. Li, L. Li, N. J. Naples, J. W. Roblee, A. Y. Yi, Micro-optical fabrication by ultraprecision diamond machining and precision molding. *Frontiers of Mechanical Engineering* **12**, 181–192 (2017).
30. S. Hatefi, K. Abou-El-Hossein, Review of single-point diamond turning process in terms of ultra-precision optical surface roughness. *The International Journal of Advanced Manufacturing Technology* **106**, 2167–2187 (2020).
31. L. J. Guo, Nanoimprint lithography: methods and material requirements. *Advanced materials* **19**, 495–513 (2007).
32. R. Kirchner, N. Chidambaram, M. Altana, H. Schift, in *Laser 3D Manufacturing IV*. (SPIE, 2017), vol. 10095, pp. 8–16.
33. C. Zheng, G. Zhao, P. So, in *SIGGRAPH Asia 2023 Conference Papers*. (2023), pp. 1–9.
34. N. Chidambaram, R. Kirchner, M. Altana, H. Schift, High fidelity 3D thermal nanoimprint with UV curable polydimethyl siloxane stamps. *Journal of Vacuum Science & Technology B* **34**, (2016).
35. M. Zhang, S. Jiang, Y. Gao, J. Nie, F. Sun, UV-nanoimprinting lithography photoresists with no photoinitiator and low polymerization shrinkage. *Industrial & Engineering Chemistry Research* **59**, 7564–7574 (2020).
36. G. Yoon, K. Kim, D. Huh, H. Lee, J. Rho, Single-step manufacturing of hierarchical dielectric metalens in the visible. *Nature communications* **11**, 2268 (2020).
37. J. A. McCoy, M. A. Verschuuren, D. M. Miles, R. L. McEntaffer, X-ray verification of sol-gel resist shrinkage in substrate-conformal imprint lithography for a replicated blazed reflection grating. *OSA Continuum* **3**, 3141–3156 (2020).
38. V. J. Einck, M. Torfeh, A. McClung, D. E. Jung, M. Mansouree, A. Arbabi, J. J. Watkins, Scalable nanoimprint lithography process for manufacturing visible metasurfaces composed of high aspect ratio TiO2 meta-atoms. *Acs Photonics* **8**, 2400–2409 (2021).
39. C. Passmore, K. E. Wu, J. R. Howse, G. Panoutsos, S. J. Ebbens, Surrogate-assisted optimization of roll-to-roll slot die coating. *Scientific Reports* **15**, 29185 (2025).
40. K. Wei, H. Romero, H. Amata, J. Sun, Q. Fu, F. Heide, W. Heidrich, Large-area fabrication-aware computational diffractive optics. *ACM Transactions on Graphics (TOG)* **44**, 1–17 (2025).
41. D. Gostimirovic, Y. Grinberg, D.-X. Xu, O. Liboiron-Ladouceur, Improving fabrication fidelity of integrated nanophotonic devices using deep learning. *ACS Photonics* **10**, 1953–1961 (2023).

42. M. M. Noack, P. H. Zwart, D. M. Ushizima, M. Fukuto, K. G. Yager, K. C. Elbert, C. B. Murray, A. Stein, G. S. Doerk, E. H. Tsai, Gaussian processes for autonomous data acquisition at large-scale synchrotron and neutron facilities. *Nature Reviews Physics* **3**, 685–697 (2021).
43. B. Lei, T. Q. Kirk, A. Bhattacharya, D. Pati, X. Qian, R. Arroyave, B. K. Mallick, Bayesian optimization with adaptive surrogate models for automated experimental design. *Npj Computational Materials* **7**, 194 (2021).
44. B. Williams, S. Cremaschi, Selection of surrogate modeling techniques for surface approximation and surrogate-based optimization. *Chemical Engineering Research and Design* **170**, 76–89 (2021).
45. D. A. Bristow, M. Tharayil, A. G. Alleyne, A survey of iterative learning control. *IEEE control systems magazine* **26**, 96–114 (2006).
46. A. Buelta, A. Olivares, E. Staffetti, W. Aftab, L. Mihaylova, A Gaussian process iterative learning control for aircraft trajectory tracking. *IEEE Transactions on Aerospace and Electronic Systems* **57**, 3962–3973 (2021).
47. T.-H. Su, M.-Y. Lou, W.-D. Xie, T.-H. Liu, S.-Z. Chen, J.-H. Jou, Synchronous Microlens Transfer-Printing Packaging for High-Efficiency Micro-LED Arrays. *ACS Applied Optical Materials*, (2026).
48. M. Kim, E. S. Oh, M. K. Kwak, Shrinkage-considered mold design for improvement of micro/nano-structured optical element performance. *Micromachines* **11**, 941 (2020).
49. I. Lim, D. J. Hoelzle, K. L. Barton, A multi-objective iterative learning control approach for additive manufacturing applications. *Control Engineering Practice* **64**, 74–87 (2017).

Supplementary Files

This is a list of supplementary files associated with this preprint. Click to download.

- 20261018MicroLensSupplementarymaterials.docx